Exploring the Granularity of the Illnesses-Related Changes in Regional Homogeneity in Major Depressive Disorder using the UKBB Data

Yewen Huang, Syed Ibrar Hussain, Demetrio Labate, Robert Azencott

Department of Mathematics, University of Houston, Houston, TX 77203, USA
Email: yhuang55@central.uh.edu, shussa44@central.uh.edu, dlabate@uh.edu, razencot@central.uh.edu

Paul Thompson

Imaging Genetics Center, Mark and Mary Stevens Neuroimaging and Informatics Institute, Keck School of Medicine, University of Southern California, Los Angeles, CA 90007, USA
Email: pthomp@usc.edu

Bhim Adhikari, Peter Kochunov

Louis A. Faillace, MD, Department of Psychiatry and Behavioral Sciences, University of Texas Health Science Center at Houston, Houston, TX 77054, USA
Email: Bhim.M.Adhikari@uth.tmc.edu, Peter.Kochunov@uth.tmc.edu

Illness related brain effects of neuropsychiatric disorders are not regionally uniform, with some regions showing large pathological effects while others are relatively spared. Presently, Big Data meta-analytic studies tabulate these effects using structural and/or functional brain atlases that are based on the anatomical boundaries, landmarks and connectivity patterns in healthy brains. These patterns are then translated to individual level predictors using approaches such as Regional Vulnerability Index (RVI), which quantifies the agreement between individual brain patterns and the canonical pattern found in the illness. However, the atlases from healthy brains are unlikely to align with deficit pattern expressed in specific disorders such as Major Depressive Disorder (MDD), thus reducing the statistical power for individualized predictions. Here, we evaluated a novel approach, where disorder specific templates are constructed using the Kullback-Leibler (KL) distance to balance granularity, signal-to-noise ratio and the contrast between regional effect sizes to maximize translatability of the population-wide illness pattern at the level of the individual. We used regional homogeneity (ReHo) maps extracted from resting state functional MRI for $N = 2,289$ MDD sample (mean age $\pm$ s.d.: 63.2 $\pm$ 7.2 years) and $N = 6104$ control subjects (mean age $\pm$ s.d.: 62.9 $\pm$ 7.2 years) who were free of MDD and any other mental condition. The cortical effects of MDD were analyzed on the 3D spherical surfaces representing cerebral hemispheres. KL-distance was used to organize the cortical surface into 28 regions of interest based on effect sizes, connectivity and signal-to-noise ratio. The RVI values calculated using this novel approach showed significantly higher effect size of the illness than these calculated using standard Desikan brain atlas.

Keywords: Kullback-Leibler Distance; Major Depressive Disorder; Neuroimaging

1. Introduction

The effects of neuropsychiatric illnesses on brain structure and function are not regionally uniform; pathological processes impact some areas while sparing others, leading to formation of illness-specific deficit patterns.[1,2] Neuroimaging can capture these deficit patterns as case-control differences in functional and structural biomarkers including cortical grey matter thickness, white matter integrity, hypoperfusion, etc. The summary of the findings is tabulated as regional effect sizes for brain areas derived from atlases that parcellate the cerebral landscape using structural landmarks, cellular organization or functional connectivity patterns. The underlying premise stems from basic neuroscience, lesion studies and functional brain mapping that shows that cortical landscape can be represented as parcels of functionally specific and interconnected areas. Large and inclusive meta-analytic studies conducted by big data consortia, such as the Enhancing Neuro Imaging Genetics through Meta-Analysis (ENIGMA) Consortium[3,4] use these maps as a principle way to report disease-related brain findings. These studies perform "Big Data" level analyses that use these summary regional deficit data aggregative findings from thousands of subjects from multiple studies/cohorts/geographic location to further refine these patterns by eliminating regionally/ethnic or site-specific heterogeneity leading to illness patterns that are reproducible across diverse cohorts.[5]

The patterns published by ENIGMA across neuropsychiatric disorders served as the basis for translating Big Data to the individual level by measuring the agreements between individual brain and those expressed in a disorder.[5] A shortcoming of this approach is that the standard atlases used by ENIGMA to summarize illness-related regional effect sizes may or may not capture the regional pattern and the granularity of the illness effects on the brain. ENIGMA uses atlases that are designed to maximize the regional contrast of the effects of neuropsychiatric illnesses. An alternative strategy is to report the effects of the illness at the spatial resolution of the neuroimaging data. However, this approach also has shortcomings: a) the voxel-wise data has much lower signal-to-noise ratio (SNR) because averaging across regions with uniform effects of the illness minimizes the noise, while maintaining the signal and b) spatial resolution, brain coverage and other data collection parameters vary from cohort to cohort, making reporting and meta-analytical aggregation a challenge. Here, we propose an alternative approach aiming to derive a disorder specific brain parcellation method that maximizes the regional ability to separate cases from controls while maximizing the SNR (through the size of the regions) and contrast between affected/unaffected areas of the brain.

We developed this approach to study the effect of major depressive disorder (MDD) on the regional homogeneity (ReHo) index to pilot this approach. MDD is the most common severe mental illness affecting up to 30% in the lifetime of the population.[6] Despite its high prevalence, the neuroimaging findings in MDD have been affected by poor reproducibility.[7] MDD does not exert a strong neurodegenerative effect on brain structure and findings of meta-analytical studies suggest that MDD is associated with only small (Cohen's $d = 0.01 - 0.1$) structural effect sizes.[8–11] Instead, the MDD-related effects on the brain are likely manifested as a reduction in regional cerebral blood flow (rCBF)[12] especially in cingulate, prefrontal and temporal areas.[13,14] ReHo is a coefficient measuring the temporal coherence of the resting state BOLD functional MRI time-series in neighboring voxels.[15,16] Lower regional ReHo in patients

with MDD versus controls are commonly reported and is often interpreted as evidence for less synchronized local neural activity/connectivity.[17-19] Interpreting the temporal correlations of BOLD signals between neighboring voxels as deficits in neural connectivity is speculative,[20,21] nonetheless, ReHo is a robust and replicable measure that has been validated in human and animal research.[22-24] We and others have shown that ReHo is physiologically linked to rCBF and about 40-60% of the variance in underlying rCBF variations.[25] We hypothesize that reduced ReHo reported in MDD captures the hypoperfusion in affected individuals.

Specifically, we show that the use of the ad-hoc MDD-specific atlas based on the maximizing the separation of regional illness effects can also maximize the translatability of the Big Data findings to the individual level by deriving the contrast between affected and unaffected areas. We chose MDD because it is associated with regionally specific reductions in cerebral blood flow (rCBF)[12] including cingulate, prefrontal and temporal areas, while other parts of the brain show no or even elevated rCBF.[13,14] Creating an ad-hoc MDD-specific brain parcellation that averages the signal across regions with consistent effect of the illnesses, based on the ability to separate cases and controls, can increase SNR and provide disorder and functionally specific pattern of illness related changes. The overall intention is to develop this parcellation approach that is based on capturing the contrast between areas that show deficits and unaffected areas for future meta-analytical studies of MDD where participating sites will use the map for reporting the effect sizes and eventually will use the combined meta-analytical effect size pattern to perform individual prediction of similarity to the illness. Specifically, we propose to use the maps to power the Regional Vulnerability Index (RVI) that measures the similarity between an individual brain and the expected patterns derived from large scale meta-analyses using a representative psychiatric illness, such as MDD.

The RVI approach assumes that the meta-analytic effect-sizes derived from such large meta-analyses can serve as the 'ground truth' for expected disorder-specific deficit patterns and that the similarity between individual and disorder pattern may serve as a biomarker. The utility of this approach has been demonstrated by showing that the white matter RVI for schizophrenia predicted treatment resistance in schizophrenia better than any individual imaging measure.[1] We later demonstrated the similarity in white matter deficit patterns across psychiatric illnesses, suggesting that RVI serves as an important index for cross-disorder research.[26,27] Here, we present an RVI that is based on the MDD-specific atlas that was built based on the regions that show effect size of MDD versus unaffected regions. Specifically, we show that optimizing the granularity of the underlying brain parcellation schema based on the balance between regional specificity and SNR can improve the power of RVI when translating these at level of the individual. Another novelty of our approach is to use the Kullback-Leibler (KL) distance – a rigorously defined distance between probability distributions – to optimize the underlying disorder-specific atlas by balancing granularity, SNR and effects of the illness.

2. Methods

Out of 22,000 available datasets from the first release, 1,780 ($\sim$ 8%) datasets were unusable, and 1,322 ($\sim$ 6%) datasets failed to pass the AFNI processing steps due to poor image quality. The usable data sample consisted of 18,898 participants (8,833 males, 10,065 females; mean age $\pm$ s.d.: 63.2 $\pm$ 7.5 years) with resting state functional MRI (rsfMRI). We used the

UKBB parser software (https://github.com/USC-IGC/ukbb_parser) to identify participants with MDD and non-psychiatric controls based on ICD codes, medication information, symptom severity, hospital records and self-reported diagnoses and other variables using previously published schema. Recurrent MDD was defined as experiencing at least two major depressive episodes in lifetime that required medication or hospitalization. Recurrent MDD subjects experienced on average 3.5 major depressive episodes in their lifetime.[28] Regional homogeneity (ReHo) maps were extracted from rsfMRI for the MDD sample (N=2,289, mean age= 63.2 ± 7.2 years) (ReHo) and control subjects (N=6,104, mean age= 62.9 ± 7.2 years) who were free of MDD and any other mental condition. Other participants were left unclassified because the definitive conclusion on certain criteria could not be made or neurological and psychiatric conditions (including stroke, cerebral ischemia or other disorders)[28] were present.

2.1. *Resting state functional MRI data acquisition, processing, analysis*

UKBB rsfMRI data were acquired on 3 T Siemens Skyra scanners with the standard Siemens 32-channel receive head coil using the following parameters: TR = 735 ms, TE = 39 ms, spatial resolution of 2.4-mm isotropic voxels, matrix size = 88 × 88 with 64 axial slices, number of volumes = 490, flip angle = 52° and multi-band acceleration factor = 8. A separate single-band reference image was acquired and used as the reference scan for head motion correction and alignment to other modalities.[29] The resting state analysis workflow developed by the ENIGMA consortium was used to process the rsfMRI data; processing steps have been described in full detail in prior publications.[30,31] The analysis workflow uses Marchenko-Pastur principal component analysis denoising[32] to improve SNR/temporal SNR of the time series data. In this workflow, a transformation is computed registering the base volume to the ENIGMA EPI template, which is used as a common anatomical spatial reference frame for registration purposes. This step was followed by 3D deconvolution of methodological covariates, and regression of the global signal.[33] Each functional volume was registered to the volume with the minimum outlier fraction for head motion correction, where each transformation was concatenated with the transformation to standard space, to avoid unnecessary interpolation. We removed the effects of the following nuisance variables by using them as covariates using multiple linear regression analysis: the six motion parameters and their temporal derivatives, and time courses from the local white matter and cerebrospinal fluid from lateral ventricles. Motion was estimated as the magnitude of displacement from one time point to the next including neighboring time points and outlier voxels fraction (> 0.1). Time points with excessive motion ($> 0.2mm$) were excluded from further statistical analysis. Images were spatially normalized to the ENIGMA EPI template in MNI standard space for group analysis. The preprocessed data was then used for ReHo calculations. In the whole sample, the average motion, average outlier voxels fraction and average time points censored fraction were 0.12 mm, 0.004 and ~ 0.13 respectively. The preprocessed data was then used for ReHo calculations.

2.2. *Regional Homogeneity (ReHo) analysis*

ReHo was designed to investigate changes in local spontaneous brain activity by performing a nearest neighbor analysis of similarity of the BOLD time-series and assigning a score, called Kendall's coefficient of concordance (KCC)[16] per voxel. The KCC score is calculated per voxel

based on signals from neighboring voxels as: $W = (\sum_i R_i^2 - nR^2)/(\frac{1}{12}K^2(n^3 - n))$. Here, W is the KCC among given voxels, ranging from 0 to 1; R_i is the sum rank of the ith time point; $R = ((n+1)K)/2$ is the mean of the R_i's; K is the number of time series within a measured cluster (K is set to be 7, 19, or 27), and n is the number of ranks (= number of volumes).[16] K was set to be 27, which is appropriate for covering all directions in 3D space and to optimize the trade-off between mitigation of partial volume effects and generation of Gaussian random fields.[17] For each subject, the ReHo map was computed in 3D volumetric space using the AFNI-command '3dReHo'. These maps were used to extract regional ReHo values for the regions of interest for post-processing.

2.3. *Computation of reference brain image and hemispheric mesh*

Clustering analyses were performed using the 2D spherical manifold defined by the hemispheric surfaces from the **average ReHo brain image** (**avBrain**), that was obtained as the arithmetic average over the entire dataset of N=8,393 (registered and normalized) ReHo images. After computing avBrain, we manually edited it to separate it into cerebrum and two hemispheres. The marching cube algorithm was used to extract uniform triangulated mesh of $K = 5068 vertices$ $\{\text{VER}_1, \text{VER}_2, \ldots, \text{VER}_K\}$ at uniform 1 mm spacing. We refer to this set of vertices as the **average boundary mesh** (**avMesh**). Each vertex VER_i in avMesh is identified by its 3 coordinates $[x_i, y_i, z_i]$ in 3D space. This procedure is illustrated in Fig. 1.
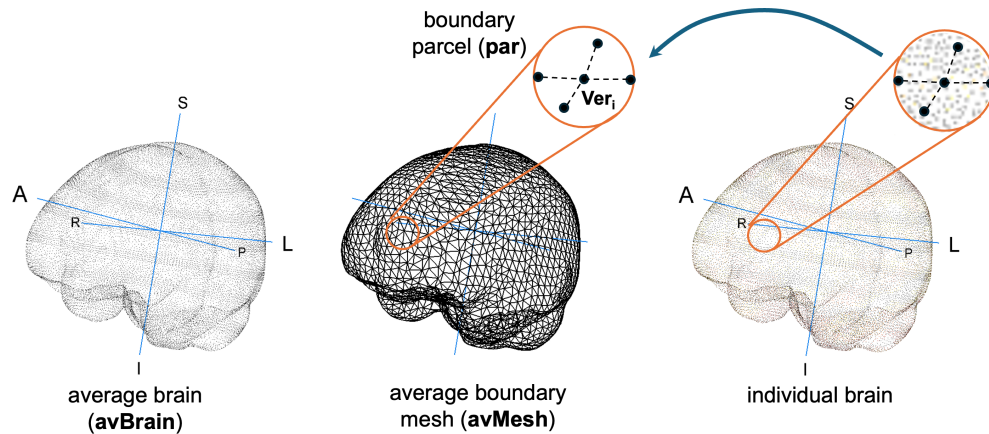

Fig. 1.   Reference brain image avBrain and a hemispheric mesh computation to generate avMesh.

2.3.1. *Registration of the average cortical mesh onto individual ReHo images*

Matching between the discretized boundary avMesh and each ReHo image $I(n)$, for a given subject n, cannot be performed using affine transformations and required a nonlinear registration where each cortical vertex VER_i of avMesh was matched to a single voxel in $I(n)$, namely the voxel of $I(n)$ that was geometrically closest to VER_i. Other common approaches to archive this registration includes averaging over a spherical kernel and averaging over the normal projection. The **intensity** $J_i(n)$ of a cortical vertex VER_i is the intensity of its matching voxel in the image $I(n)$. After registration was completed for all vertices of the average boundary

mesh avMesh, then each subject could be characterized by a boundary pattern $J(n)$ where each cortical vertex VER_i of avMesh has the image intensity $J_i(n)$ computed via registration. That is, the $n-$th subject is described by a list of K numerical features, i.e., the K intensities $\{J_1(n), J_2(n), \ldots, J_K(n)\}$ indexed by the K cortical vertices $\{VER_1, VER_2, \ldots, VER_K\}$ on the average boundary mesh avMesh.

2.4. *Parcellation of the average boudary mesh: SNR vs. granularity*

For each cortical vertex VER_i on avMesh, we computed three **boundary parcels** $parD(i)$ centered at VER_i and having three different sizes $D = 1, 3, 5$, to capture local information in the ReHo image at different **granularity levels**.

The parcel $parD(i)$ includes the D closest neighbors of the vertex VER_i in avMesh. Hence, parcel $par1(i)$ only contains the boundary vertex VER_i, parcel $par3(i)$ contains VER_i and its 2 closest neighbors in avMesh and $par5(i)$ contains VER_i and its 4 closest neighbors in avMesh. The radius of $par3(i)$ roughly ranges between 1 and 3.1 voxels with a mean radius of 1.9 voxels; for $par5(i)$, the parcel radius ranges between 1.4 and 3.6 voxels, with a mean radius of 2.5 voxels.

2.5. *Kullback-Leibler distance between two probability distributions*

Let us consider two multivariate probability distributions P and Q on $\mathbb{R}^D$; for instance, P and Q can be determined by two probability density functions $f_P(x)$ and $f_Q(x)$ defined for $x \in \mathbb{R}^D$. The **Kullback-Leibler (KL) divergence**[34,35] between P and Q, denoted as $KL(P,Q)$, classically measures how much Q differs from P. When the density functions f_P and f_Q are known, the KL divergence $KL(P,Q)$ is given by the explicit formula

$$KL(P,Q) = \int f_P(x) \log \frac{f_P(x)}{f_Q(x)} dx \geq 0.$$

Note that $KL(P,Q) \neq KL(Q,P)$ in general. One defines a symmetric **KL distance**[36] between P and Q by the formula:

$$KLdis(P,Q) = KLdis(Q,P) = KL(P,Q) + KL(Q,P) \geq 0.$$

We have that $KLdis(P,Q) = 0$ if and only if $P = Q$

The KL distance has played a key part in theoretical and applied statistics for more than 40 years.[37] It quantifies the discriminating power of the well-known log-likelihood statistical test to discriminate between two probability models P and Q based on N random observed vectors $x_1, \ldots, x_N$ of dimension D generated by an unknown probability distribution. This log-likelihood test between P and Q is an *optimal test* that is based on comparing the log-likelihood of observations $x_1, \ldots, x_N$ under P with their log-likelihood under Q. As such it provides a most sensitive measure to compare signal intensities over multiple locations.

When the probability distributions P and Q have multivariate normal density functions $f_P(x)$ and $f_Q(x)$, respectively, defined for all $x \in \mathbb{R}^D$, then f_P and f_Q are determined by their respective mean vectors m_P, m_Q and their $D \times D$ covariance matrices S_P, S_Q. In this case, the KL distance between P and Q is computed using the explicit formula:

$$KLdis(P,Q) = -D + \frac{1}{2}trace(S_P^{-1}S_Q + S_Q^{-1}S_P) + \frac{1}{2}(m_P - m_Q)^T(S_Q^{-1}S_P^{-1})(m_P - m_Q)$$

where A^T denotes the transpose of matrix A.

2.6. *Discriminating score of boundary parcels*

Within the average boundary mesh avMesh, we intend to identify which small cortical parcels $parD(i)$, $D = 1, 3, 5$, have high discriminating power between CTL and MDD subjects. To this end, for each parcel, we introduce a notion of discriminating score as follows.

For any vertex VER_i and boundary parcel $parD(i)$ of size D centered around VER_i, the boundary vertices belonging to $parD(i)$ are indexed by their D indices $i1, i2, \ldots, iD$, with $i1 = i$. For the n-th subject, these D vertices define a vector $W_i(n)$ of D intensities pre-computed above by registration of avMesh to the subject's ReHo image $I(n)$. Namely we set $W_i(n) = [J_{i1}(n), J_{i2}(n), \ldots, J_{iD}(n)]$.

Hence, we define two subsets of vectors H_1 and H_0 in $\mathbb{R}^D$ of respective sizes N_1 and N_0 ($N_1 = 2,289$, $N_0 = 6,104$, here) by:

- H_1 = set of all vectors $W_i(n)$ such that subject n belongs to the MDD class
- H_0 = set of all vectors $W_i(n)$ such that subject n belongs to the CTL class

The $N_1 = 2,289$ observed vectors $W_i(n)$ in H_1 will be viewed as a sample of N_1 random vectors generated by a multivariate normal P_1 with mean vector m_1 and $D \times D$ covariance matrix S_1. Similarly, the $N_0 = 6,104$ vectors $W_i(n)$ in H_0 provide a sample of size N_0 generated by a multivariate normal P_0 with mean vector m_0 and $D \times D$ covariance matrix S_0. The vectors m_0, m_1 and the matrices S_0, S_1 are unknown but can be estimated by the following sample means and sample covariances:

$$m_\ell = \frac{1}{N_\ell} \sum_{W_i(n) \in H_\ell} W_i(n), \ \ cov_\ell = \frac{1}{N_\ell} \sum_{W_i(n) \in H_\ell} (W_i(n) - m_\ell)(W_i(n) - m_\ell)^T, \ \ \text{for } \ell = 0, 1.$$

When $KLdis(P_1, P_0)$ is large, the two probabilities P_1 and P_0 are very different, meaning that the boundary parcel $parD(i)$ has potentially high discriminating power between the CTL and MDD groups. Hence, we define the **discriminating score** $scoreD(i)$ of boundary parcel $parD(i)$ as the KL distance $KLdis(P_1, P_0)$ computed above. Clearly, the computation of $scoreD(i)$ for parcel $parD(i)$ need to be repeated separately for each boundary vertex VER_i, where $i = 1, \ldots, K$. This yielded $K = 5,020$ discriminating scores $scoreD(i)$ at granularity sizes $D = 1, 3, 5$, with one score per boundary vertex VER_i. We can then re-order the vertices VER_i in decreasing order of their discriminating scores and display them in 3D space on the average boundary mesh avMesh. We applied the method described for granularity sizes $D = 1, 3, 5$.

2.7. *Implementation of discriminating score analysis*

The methods outlined above required about 20 hours of computing time on a standard laptop to compute the three discriminating scores $scoreD(i)$, $D = 1, 3, 5$, for each one of the $K = 5,020$ boundary vertices VER_i generated at scale 5x5x5. This led to a positive first assessment of our methodology at a reasonable computing cost, and a substantial analysis of the spatial continuity of our 3 discriminating scores.

Since the brain ReHo images of our UKBB-MDD dataset and the corresponding average brain images were actually discretized at a finer scale 2x2x2 (mm), we have then used the freely

available Mango software[38] to generate, at scale 2x2x2, a new triangulated mesh avMesh2 of $L = 20,025$ boundary vertices Z_s, $s = 1, 2, \ldots, L$, densely located on the boundary of the average brain. Of course, avMesh2 contained our initial coarser avMesh of $K = 5,020$ boundary vertices VER_i, $i = 1, 2, \ldots, K$, discretizing the brain boundary at scale 5x5x5.

Our three discriminating $scoreD(i)$, $D = 1, 3, 5$, initially computed for each VER_i of avMesh were then smoothly extended to scores $scoreD(i)$, $D = 1, 3, 5$, for each Z_s of avMesh2 using the following fast spatial propagation algorithm. Specifically, for each vertex Z_s of avMesh2, we identified the list $G(s)$ of all vertices VER_i in avMesh which are at distance less than 5 mm from Z_s, and computed the discriminating score $scoreD(s)$ of Z_s as the average of $scoreD(i)$ over all vertices VER_i belonging to $G(s)$; this procedure was carried out for $D = 1, 3, 5$. This method for spatial extension was useful to generate better 3D visualizations of the most significant discriminating brain boundary vertices on avBrain.

2.8. *Regional Vulnerability Index (RVI) calculations*

RVI scores were calculated using the 'RVIpkg' in the R software based on our previous publication[39] with some revisions. The original RVI calculated the correlational agreement between an individual's regional brain measures and the pattern of regional MDD-related brain calculated using a standard atlas.[5] Here, we used the regions identified by the cluster analysis to compute the effect sizes for MDD cases vs. controls. Next, we used these effect sizes to calculate RVI for each subject as the dot product between vectors $Z = (Z_i)$ and $E = (E_i)$, normalized by the dimensions of the vector using the equation $RVI = \sum_{i=1}^{N} Z_i E_i$, where Z is the vector of deviation from the mean and E is the vector of meta-analytical effect size (*Cohen's d coefficients*) for the i-th regional measure for MDD. N is the dimension of the vector, i.e., the total number of imaging phenotypes for that modality. The modified RVI was calculated for the whole-brain phenotype vector and for cortical, subcortical and white matter modalities. Positive RVI values indicate that the regional pattern of an individual coincides with the expected pattern of MDD based on the overall effect sizes. We compared effect sizes for the RVI-MDD vs. the effect sizes obtained for individual regions identified by cluster analysis.

3. Results

3.1. *Calculation of discriminatory boundary vertices*

According to the procedure described in Sec. 2.3, for each one of the $K = 5,020$ vertices VER_i from the brain boundary mesh, we computed three discriminating scores, namely, $score1(i)$, $score3(i)$, $score5(i)$, corresponding to the boundary parcels $par1(i), par2(i), par5(i)$ of sizes $D = 1, 3$ and 5, respectively, centered at each boundary vertex VER_i. As explained above, these scores *quantify the discriminating power of statistical tests based on log-likelihood values*, using boundary parcels of different sizes. We implemented numerical simulations to compute the respective statistical significance thresholds $thr1, thr3, thr5$ for $score1(i), score3(i), score5(i)$. For instance, whenever $score3(i) < thr3$, then vertex VER_i has high probability of *being not discriminatory* between the CTL and MDD groups. Table 1 reports the minimum (min), median or 50%-quantile, 80%-quantile, significant thresholds (threshold) of the computed discriminating scores and finally the percentages of significant mesh boundary vertices for

$score1, score3, score5$. We note that the highest percentage (30%) of significant vertices is reached with $score3$.

Table 1. Discriminating scores for granularity sizes 1, 3 and 5.

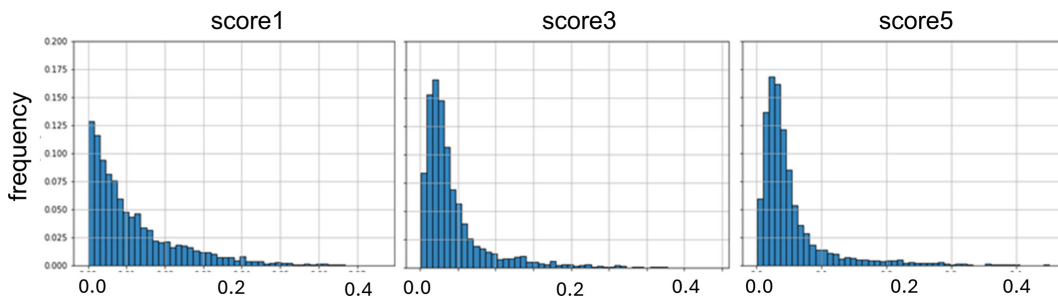|	min	median	80% quant	threshold	significant vertices (%)
score1	0	.009	.020	.015	27%
score3	0	.030	.051	.045	30%
score5	0	.040	.070	.070	20%

Fig. 2. Histograms of the discriminating scores $score1, score3, score5$ computed from the 5,020 brain boundary vertices VER_i of avMesh. Each plot displays horizontally the values of the discriminating score and vertically the associated frequencies.

Fig. 2 displays the histograms of the discriminating scores $score1, score3, score5$. The figure shows that the distribution of $score1$, which has a peak at $score1 = 0$, is very different from the distributions of $score3$ and $score5$. In fact, after horizontal rescaling of scores values, the distributions of $score3$ and $score5$ become similar. This remark is confirmed by the calculation of the correlation matrix of $score1, score3, score5$, showing that $score3$ and $score5$ are highly correlated (corr $= 0.89$), while $score1$ is weakly correlated to either $score3$ or $score5$.

3.1.1. *Spatial stability of discriminating scores*

Clearly, the value of the discriminating score $scoreD(i)$ computed at a vertex VER_i may be sensitive to the granularity size D. To address this problem, we proceeded as follows.

For each brain boundary vertex VER_i in avMesh, we denote as VER_{i*} its closest neighbor within avMesh and let $d(i)$ be the Euclidean distance between vertices VER_i and VER_{i*}.

For each vertex VER_i and any dimension D, the relative change $relchD(i)$ of the discriminating score $scoreD(i)$ when one replaces VER_i by its closest neighbor VER_{i*} is defined by $relchD(i) = \frac{|scoreD(i) - scoreD(i*)|}{scoreD(i)}$. To quantify the *spatial stability* of $scoreD(i)$ around a boundary vertex VER_i, we compute its Lipschitz coefficient $LipD(i) = \frac{relchD(i)}{d(i)}$, measuring the sensitivity of the discriminating score to small spatial changes. Hence, for each discriminating score, *lower values of its Lipschitz coefficients indicate higher spatial stability of the score.*

Fig. 3(a) displays the histograms of $Lip1(i), Lip2(i), Lip3(i)$ and shows that $Lip1(i)$ is stochastically larger than $Lip3(i)$ or $Lip5(i)$. This implies that $score1$ is significantly less spatially stable than $score3$ and $score5$. This observation is consistent with the plots of the three
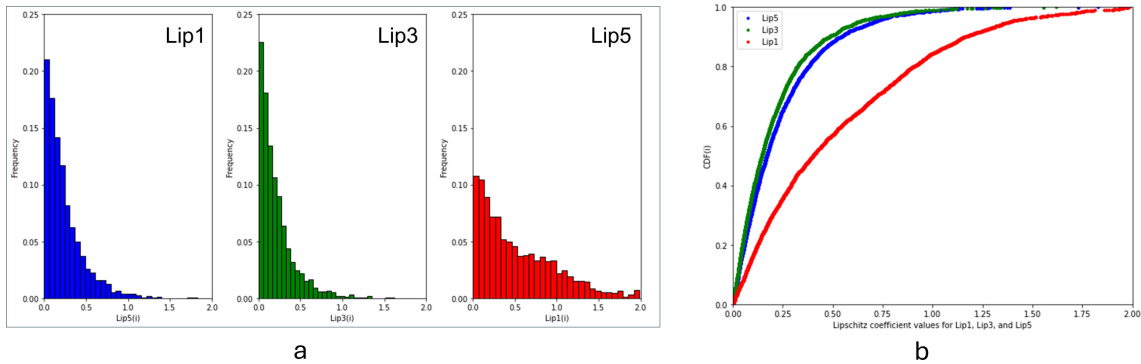
Fig. 3. (a) Histograms of the Lipschitz coefficients $Lip1$, $Lip3$ and $Lip5$ of the discriminating scores $score1$, $score3$, and $score5$, respectively; (b) corresponding cumulative distribution functions of $Lip1$, $Lip3$ and $Lip5$. Plots show that $score1$ is significantly less spatially stable than $score3$ or $score5$.

Cumulative Distribution Functions of LipD, for D=1,2,3, denoted as CDFD and shown in Fig. 3(b). The figure shows that, for all $x = LipD$, one has that $CDF1(x) \leq CDF3(x)$ and $CDF1(x) \leq CDF5(x)$, again confirming that $score1$ is significantly less spatially stable than $score3$ and $score5$. In fact, the plot in Fig. 3(b) confirms that $score3$ is stochastically the most spatially stable of the 3 scores computed.

3.2. *3D visualization of discriminatory boundary vertices*

Based on the analysis presented above, we concluded that $score3$, at granularity size $D = 3$, is the most spatially stable, in a precise mathematical sense, hence providing the most valuable information about which boundary vertices have most discriminatory power. This granularity size was shown perform better than granularity sizes $D = 1$ and $D = 5$. We focus henceforth on this granularity size to report our graphic illustration of the most discriminatory boundary vertices. Accordingly, Fig. 4 displays the boundary vertices having highest discriminatory score using $score3$, the discriminating score computed at granularity size $D = 3$, overlaid on rendered brain.

3.3. *Score based parcellation of brain boundary and RVI results*

Using the Mango software on avBrain at scale 2x2x2, we generated a triangulated mesh avMesh2 of 20,025 vertices and, for each such vertex, we computed a discriminating score, namely score3, as seen above.

The triangulated mesh avMesh2 contained p triangles $\{TR_1, \ldots, TR_p\}$, with roughly $p \approx 40,000$. We extended our discriminating score3 to each triangle TR_j, by computing the average of the scores of the 3 vertices of TR_j. After reordering the list of our p triangles in decreasing order of their discriminating scores, we partitioned this ordered list of triangles into 6 successive sub-lists $S_1, S_2, \ldots, S_6$ of similar sizes, ranging from $6,000$ to $7,000$ triangles. Next, for each $i = 1, \ldots, 6$ we computed disjoint "watertight" connected components of the sub-list S_i. Recall that a set W of triangles is called watertight connected if any two triangles T and T' in W can be linked by some chain of triangles $T_1 = T, T_2, \ldots, T_r = T'$ where any pair of successive triangles have one edge in common, and where r is any integer.

After completion of this procedure, for each sub-list S_i, we obtained a partition of our
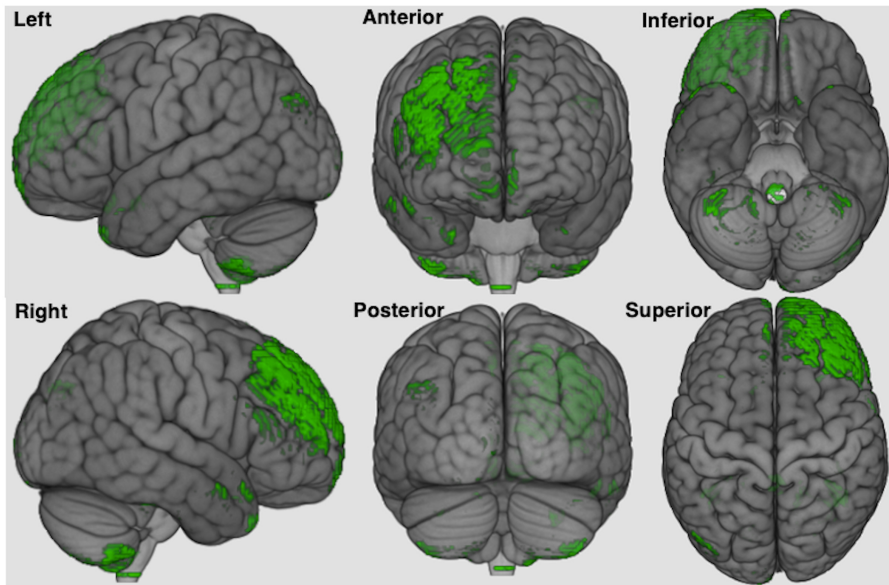
Fig. 4. Boundary vertices with highest discriminating scores (using score3 above 80% quartile), overlaid on rendered brain with different views.

initial set of p triangles into q disjoint watertight connected components $C_1, \ldots, C_q$. Each C_s is a finite set of small triangles on the surface of the average brain, defining a connected sub-region REG_s of the brain surface. We kept only the regions REG_s which have a large enough area (i.e., more than 250 vertices) and implemented a simple procedure for pragmatic regrouping of the very small sub-regions. At this point we obtained a score-based parcellation of the brain surface into sub-regions denoted REG_s, which we used to compute RVI values.

3.4. *Effect sizes for ReHo values in clusters vs. RVI*

The Cohen's d effect sizes were calculated for the 28 spatial distinct components that were identified based on the ability to discriminated between MDD cases and controls and were larger than 200 connected vertices. The effect sizes varied from $d = 0.25, p = 10^{-24}$ for the ReHo values calculated for the highly discriminating component in Fig. 4 to $d = 0.00, p = 1.00$ for the component that showed no effects of MDD. We next calculated the individual RVI using the effect sizes for the 28 components. Subjects with MDD showed highly elevated RVI-MDD versus controls (0.16 ± 0.01 vs -0.01 ± 0.01), Cohen's $d = 0.36, p = 10^{-55}$. We observed that the effect size for RVI were numerically stronger than effect sizes for any of the individual components, as shown in Fig. 5.

4. Discussion

Regional cerebral hypoperfusion in individuals with MDD was first described over three decades ago.[14,40,41] Specifically, with the hypoperfusion of limbic-frontal-temporal circuitry,[42] this approach was deemed replicable, informative of the clinical state and predictive of treatment outcome.[14,43] Our study proposes and evaluates a novel approach to categorize and parcellate the cortical landscape based on the balance between the size of the continuous region and the effect size to discriminate between cases and controls. This method achieves the
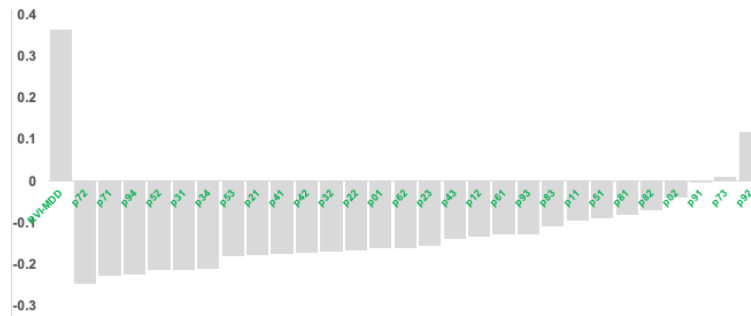
Fig. 5. Effect-size of RVI compared to effect-size for individual components. For instance, the component p_{11} represents the first parcellated region and the first cluster and and p_{01} represents the tenth parcellated region and the first cluster respectively.

optimal granularity to quantify the effects of the illness on the brain that maintains high SNR while preserving functional specificity to the areas that show effects of the illness. The proposed methodologies can be viewed as development of a disorder specific atlas that is focused on subdivision of the overall cerebral cortex into a set of 10 levels based on their ability to discriminate cases versus controls. This regional variability in effect sizes is then used to build a novel biomarker - RVI - that summarizes the agreement between individual brain patterns and the expected pattern of the illness. We found that the RVI built on these regions showed numerically higher effect size of the illness than the best effect sizes (level 1) for regional measures (Cohen's d=0.36 versus 0.25). This suggested that individual agreement with the pattern served as a better phenotype than hypoperfusion in any single area of the brain, even those specifically chosen to provide the best description.

We showed that effects of the ReHo-based measurements can be used to summarize hypoperfusion patterns in MDD. The granularity analyses demonstrated that areas with best discrimination between MDD cases and controls involve middle and inferior frontal and parietal regions that were previously identified by PET and SPECT studies.[44,45] However, the effect sizes for these regions were modest ($\sim$0.22-0.25) suggesting that the lower ReHo values in these areas in an individual are not specific to MDD and are unlikely to have clinical relevance; a further detailed study on the clinical significance of these findings will be needed. In contrast, the ReHo-based RVI for MDD built on the overall contrast across all ten levels showed significant elevation in individuals with MDD and overall had numerically larger effect sizes than these for regional ReHo. The RVI approach is not new or specific to ReHo. It was first applied in schizophrenia, where higher RVI values for schizophrenia have been linked to treatment resistance, cognitive deficits, to family risks for the disease[2,5,5,39] and was shown to be applicable to other illnesses or conditions.[46,47] The RVI approach has been proposed as a prospective tool for early detection of brain patterns shifting towards a particular condition, and may provide an early predictive signal for other neurological and psychiatric illnesses.[39,48] However, all previous work was focused on structural brain deficits. The novelty of this work is to show the applicability of RVI for functional fMRI measures, here using ReHo, which we posited as a proxy for rCBF signal and can potentially be altered by therapies such as medication. It is also novel because the RVI was built on the regional measurements that were

specifically identified for this purpose and balanced the size of the regions versus the disorder related contrast. Still, how RVI measures derived using ReHo correlate with clinical measures of MDD severity and whether there exist identifiable brain regions or patterns need to be explored.

There are limitations to this study. This analysis was focused on evaluation of the MDD-specific versus cortical-area parsed parcellation to tabulate effect sizes of MDD for further RVI analyses. Future studies need to evaluate MDD-specific versus other connectivity-atlases. It is likewise important to evaluate the ability of RVI calculated using MDD-specific versus standard atlas approaches to predict clinical and cognitive variance among subjects. We calculated rsfMRI ReHo signal that included global signal regression (GSR). The global signal in rsfMRI data is associated with head motion, respiration and cardiac rhythms.[49,50] GSR is a necessary pre-processing step for ReHo analysis because these non-physiological factors can artifactually increase ReHo through global autocorrelation[51,52] and exerts complex effects on ReHo measures.[19,53] However, other studies demonstrated that GSR also carries diagnosis related variance.[54–56] No analyses were performed to examine whether our study findings would differ without GSR, a shortcoming of the rsfMRI data processing. In addition, testing of the outcomes in this study were limited to subjects in the same cohort. The narrow aim of this study was to evaluate the novel parcellation approach and show that RVI derived from these regions carried higher effect size than the regions specifically selected for their high discrimination of illness effect. Follow up studies will evaluate if the pattern of MDD ReHo contrasts can be replicated in other cohorts and further this pattern by performing meta-aggregation to improve this disorder specific parcellation schema. In addition, our analysis did not focus on MDD subtypes and this need to be considered in future studies.

The method presented in the manuscript can be extended to other types of neuropsychiatric disorders where similar datasets are available with minimal changes. Future studies need to examine the granularity size more extensively to allow for a wider range of scales. From the viewpoint of computational cost, the method presented is scalable as the most computationally expensive steps of the algorithm, namely vertex registration and score computation, are highly parallelizable.

Acknowledgments

References

1. P. Kochunov, P. M. Thompson and L. E. Hong, Toward high reproducibility and accountable heterogeneity in schizophrenia research, *JAMA Psychiatry* **76**, 680 (2019).
2. P. Kochunov, F. Fan, M. C. Ryan, K. S. Hatch, S. Tan, N. Jahanshad, P. M. Thompson, T. G. van Erp, J. A. Turner, S. Chen *et al.*, Translating ENIGMA schizophrenia findings using the regional vulnerability index: association with cognition, symptoms, and disease trajectory, *Human Brain Mapping* **43**, 566 (2022).
3. P. M. Thompson, O. A. Andreassen, A. Arias-Vasquez, C. E. Bearden, P. S. Boedhoe, R. M.

Brouwer, R. L. Buckner, J. K. Buitelaar, K. B. Bulayeva, D. M. Cannon *et al.*, ENIGMA and the individual: Predicting factors that affect the brain in 35 countries worldwide, *Neuroimage* **145**, 389 (2017).

4. P. M. Thompson, N. Jahanshad, C. R. Ching, L. E. Salminen, S. I. Thomopoulos, J. Bright, B. T. Baune, S. Bertolín, J. Bralten, W. B. Bruin *et al.*, ENIGMA and global neuroscience: A decade of large-scale studies of the brain in health and disease across more than 40 countries, *Translational Psychiatry* **10**, p. 100 (2020).

5. P. Kochunov, J. Huang, S. Chen, Y. Li, S. Tan, F. Fan, W. Feng, Y. Wang, L. M. Rowland, A. Savransky *et al.*, White matter in schizophrenia treatment resistance, *American Journal of Psychiatry* **176**, 829 (2019).

6. P. Waraich, E. M. Goldner, J. M. Somers and L. Hsu, Prevalence and incidence studies of mood disorders: a systematic review of the literature, *The Canadian Journal of Psychiatry* **49**, 124 (2004).

7. J. P. Ioannidis, How to make more published research true, *Revista Cubana de Información en Ciencias de la Salud (ACIMED)* **26**, 187 (2015).

8. M. Farrell, T. Werge, P. Sklar, M. J. Owen, R. Ophoff, M. C. O'Donovan, A. Corvin, S. Cichon and P. F. Sullivan, Evaluating historical candidate genes for schizophrenia, *Molecular psychiatry* **20**, 555 (2015).

9. Subcortical brain alterations in major depressive disorder: findings from the ENIGMA Major Depressive Disorder Working Group.

10. L. Schmaal, D. Hibar, P. G. Sämann, G. Hall, B. Baune, N. Jahanshad, J. Cheung, T. G. van Erp, D. Bos, M. A. Ikram *et al.*, Cortical abnormalities in adults and adolescents with major depression based on brain scans from 20 cohorts worldwide in the ENIGMA Major Depressive Disorder Working Group, *Molecular psychiatry* **22**, 900 (2017).

11. S. Kelly, N. Jahanshad, A. Zalesky, P. Kochunov, I. Agartz, C. Alloza, O. Andreassen, C. Arango, N. Banaj, S. Bouix *et al.*, Widespread white matter microstructural differences in schizophrenia across 4322 individuals: results from the ENIGMA schizophrenia DTI working group, *Molecular psychiatry* **23**, 1261 (2018).

12. J. P. Gray, V. I. Müller, S. B. Eickhoff and P. T. Fox, Multimodal abnormalities of brain structure and function in major depressive disorder: a meta-analysis of neuroimaging studies, *American Journal of Psychiatry* **177**, 422 (2020).

13. K. Matsuo, D. Glahn, M. Peluso, J. Hatch, E. Monkul, P. Najt, M. Sanches, F. Zamarripa, J. Li, J. Lancaster *et al.*, Prefrontal hyperactivation during working memory task in untreated individuals with major depressive disorder, *Molecular Psychiatry* **12**, 158 (2007).

14. H. S. Mayberg, S. K. Brannan, R. K. Mahurin, P. A. Jerabek, J. S. Brickman, J. L. Tekell, J. A. Silva, S. McGinnis, T. G. Glass, C. C. Martin *et al.*, Cingulate function in depression: a potential predictor of treatment response, *Neuroreport* **8**, 1057 (1997).

15. L. Wang, M. Song, T. Jiang, Y. Zhang and C. Yu, Regional homogeneity of the resting-state brain activity correlates with individual intelligence, *Neuroscience letters* **488**, 275 (2011).

16. Y. Zang, T. Jiang, Y. Lu, Y. He and L. Tian, Regional homogeneity approach to fMRI data analysis, *Neuroimage* **22**, 394 (2004).

17. L. Jiang and X.-N. Zuo, Regional homogeneity: a multimodal, multiscale neuroimaging marker of the human connectome, *The Neuroscientist* **22**, 486 (2016).

18. C. Qiu, W. Liao, J. Ding, Y. Feng, C. Zhu, X. Nie, W. Zhang, H. Chen and Q. Gong, Regional homogeneity changes in social anxiety disorder: a resting-state fMRI study, *Psychiatry Research: Neuroimaging* **194**, 47 (2011).

19. X.-N. Zuo, T. Xu, L. Jiang, Z. Yang, X.-Y. Cao, Y. He, Y.-F. Zang, F. X. Castellanos and M. P. Milham, Toward reliable characterization of functional homogeneity in the human brain: preprocessing, scan duration, imaging resolution and computational space, *Neuroimage* **65**, 374

(2013).

20. H. Li, Y. Lin, J. Chen, X. Wang, Q. Wu, Q. Li and Z. Chen, Abnormal regional homogeneity and functional connectivity in adjustment disorder of new recruits: a resting-state fMRI study, *Japanese journal of radiology* **35**, 151 (2017).

21. J. Chen, Y. Xu, K. Zhang, Z. Liu, C. Xu, Y. Shen and Q. Xu, Comparative study of regional homogeneity in schizophrenia and major depressive disorder, *American Journal of Medical Genetics Part B: Neuropsychiatric Genetics* **162**, 36 (2013).

22. Y. Han, J. Wang, Z. Zhao, B. Min, J. Lu, K. Li, Y. He and J. Jia, Frequency-dependent changes in the amplitude of low-frequency fluctuations in amnestic mild cognitive impairment: a resting-state fMRI study, *Neuroimage* **55**, 287 (2011).

23. Z. Zhang, Y. Liu, T. Jiang, B. Zhou, N. An, H. Dai, P. Wang, Y. Niu, L. Wang and X. Zhang, Altered spontaneous activity in alzheimer's disease and mild cognitive impairment revealed by Regional Homogeneity, *Neuroimage* **59**, 1429 (2012).

24. L. Jiang, Y. Xu, X. Zhu, Z. Yang, H. Li and X. Zuo, Local-to-remote cortical connectivity in early-and adulthood-onset schizophrenia, *Translational Psychiatry* **5**, e566 (2015).

25. J. Zhu, Y. Jin, K. Wang, Y. Zhou, Y. Feng, M. Yu and X. Jin, Frequency-dependent changes in the regional amplitude and synchronization of resting-state functional MRI in stroke, *PLoS One* **10**, p. e0123850 (2015).

26. P. Kochunov, L. E. Hong, E. L. Dennis, R. A. Morey, D. F. Tate, E. A. Wilde, M. Logue, S. Kelly, G. Donohoe, P. Favre *et al.*, ENIGMA-DTI: Translating reproducible white matter deficits into personalized vulnerability metrics in cross-diagnostic psychiatric research, *Human Brain Mapping* **43**, 194 (2022).

27. P. Kochunov, A. Zavaliangos-Petropulu, N. Jahanshad, P. M. Thompson, M. C. Ryan, J. Chiappelli, S. Chen, X. Du, K. Hatch, B. Adhikari *et al.*, A white matter connection of schizophrenia and Alzheimer's disease, *Schizophrenia Bulletin* **47**, 197 (2021).

28. D. J. Smith, B. I. Nicholl, B. Cullen, D. Martin, Z. Ul-Haq, J. Evans, J. M. Gill, B. Roberts, J. Gallacher, D. Mackay *et al.*, Prevalence and characteristics of probable major depression and bipolar disorder within UK biobank: cross-sectional study of 172,751 participants, *PloS One* **8**, p. e75362 (2013).

29. F. Alfaro-Almagro, M. Jenkinson, N. K. Bangerter, J. L. Andersson, L. Griffanti, G. Douaud, S. N. Sotiropoulos, S. Jbabdi, M. Hernandez-Fernandez, E. Vallee *et al.*, Image processing and Quality Control for the first 10,000 brain imaging datasets from UK Biobank, *Neuroimage* **166**, 400 (2018).

30. B. M. Adhikari, N. Jahanshad, D. Shukla, D. C. Glahn, J. Blangero, P. T. Fox, R. C. Reynolds, R. W. Cox, E. Fieremans, J. Veraart *et al.*, Comparison of heritability estimates on resting state fMRI connectivity phenotypes using the ENIGMA analysis pipeline, *Human Brain Mapping* **39**, 4893 (2018).

31. B. M. Adhikari, N. Jahanshad, D. Shukla, D. C. Glahn, J. Blangero, R. C. Reynolds, R. W. Cox, E. Fieremans, J. Veraart, D. S. Novikov *et al.*, Heritability estimates on resting state fmri data using ENIGMA analysis pipeline, in *Pacific Symposium on Biocomputintg 2018: Proceedings of the Pacific Symposium*, 2018.

32. J. Veraart, D. S. Novikov, D. Christiaens, B. Ades-Aron, J. Sijbers and E. Fieremans, Denoising of diffusion MRI using random matrix theory, *Neuroimage* **142**, 394 (2016).

33. B. M. Adhikari, N. Jahanshad, D. Shukla, J. Turner, D. Grotegerd, U. Dannlowski, H. Kugel, J. Engelen, B. Dietsche, A. Krug *et al.*, A resting state fmri analysis pipeline for pooling inference across diverse cohorts: an ENIGMA rs-fMRI protocol, *Brain Imaging and Behavior* **13**, 1453 (2019).

34. M. Tumminello, F. Lillo and R. N. Mantegna, Kullback-Leibler distance as a measure of the information filtered from multivariate data, *Physical Review E—Statistical, Nonlinear, and Soft*

Matter Physics **76**, p. 031123 (2007).

35. F. Pérez-Cruz, Kullback-Leibler divergence estimation of continuous distributions, in *2008 IEEE international symposium on information theory*, 2008.

36. D. H. Johnson, S. Sinanovic *et al.*, Symmetrizing the Kullback-Leibler distance, *IEEE Transactions on Information Theory* **1**, 1 (2001).

37. J. Shlens, Notes on Kullback-Leibler divergence and likelihood theory, *Systems Neurobiology Laboratory* **92037**, 1 (2007).

38. Mango (Multi-image Analysis GUI) `https://mangoviewer.com/`, [Accessed 10-08-2024].

39. P. Kochunov, Y. Ma, K. S. Hatch, S. Gao, A. Acheson, N. Jahanshad, P. M. Thompson, B. M. Adhikari, H. Bruce, J. Chiappelli *et al.*, Ancestral, pregnancy, and negative early-life risks shape children's brain (dis) similarity to schizophrenia, *Biological Psychiatry* **94**, 332 (2023).

40. H. S. Mayberg, P. J. Lewis, W. Regenold and H. N. Wagner, Paralimbic hypoperfusion in unipolar depression, *Journal of Nuclear Medicine* **35**, 929 (1994).

41. H. Mayberg, Depression and frontal-subcortical circuits: Focus on prefrontal-limbic interactions. (2001).

42. A. Silva-dos Santos, M. Sales, A. Sebastião and R. Gusmão, A new viewpoint on the etiopathogenesis of depression: insights from the neurophysiology of deep brain stimulation in Parkinson's disease and treatment-resistant depression, *Frontiers in Psychiatry* **12**, p. 607339 (2021).

43. D. G. Amen and M. Easton, A new way forward: how brain SPECT imaging can improve outcomes and transform mental health care into brain health care, *Frontiers in Psychiatry* **12**, p. 715315 (2021).

44. K. Helm, K. Viol, T. M. Weiger, P. A. Tass, C. Grefkes, D. Del Monte and G. Schiepek, Neuronal connectivity in major depressive disorder: a systematic review, *Neuropsychiatric disease and treatment* , 2715 (2018).

45. S.-G. Kang and S.-E. Cho, Neuroimaging biomarkers for predicting treatment response and recurrence of major depressive disorder, *International journal of molecular sciences* **21**, p. 2148 (2020).

46. P. Kochunov, Y. Ma, K. S. Hatch, L. Schmaal, N. Jahanshad, P. M. Thompson, B. M. Adhikari, H. Bruce, J. Chiappelli, E. L. Goldwaser *et al.*, Separating clinical and subclinical depression by big data informed structural vulnerability index and its impact on cognition: ENIGMA Dot Product, in *Pacific Symposium on Biocomputing. Pacific Symposium on Biocomputing*, 2022.

47. K. S. Hatch, S. Gao, Y. Ma, A. Russo, N. Jahanshad, P. M. Thompson, B. M. Adhikari, H. Bruce, A. Van der Vaart, A. Sotiras *et al.*, Brain deficit patterns of metabolic illnesses overlap with those for major depressive disorder: A new metric of brain metabolic disease, *Human Brain Mapping* **44**, 2636 (2023).

48. N. R. Karcher, H. Modi, P. Kochunov, S. Gao and D. M. Barch, Regional vulnerability indices in youth with persistent and distressing psychoticlike experiences, *JAMA Network Open* **6**, e2343081 (2023).

49. R. M. Birn, J. B. Diamond, M. A. Smith and P. A. Bandettini, Separating respiratory-variation-related fluctuations from neuronal-activity-related fluctuations in fMRI, *Neuroimage* **31**, 1536 (2006).

50. J. D. Power, A. Mitra, T. O. Laumann, A. Z. Snyder, B. L. Schlaggar and S. E. Petersen, Methods to detect, characterize, and remove motion artifact in resting state fMRI, *Neuroimage* **84**, 320 (2014).

51. J. D. Kruschwitz, A. Meyer-Lindenberg, I. M. Veer, C. Wackerhagen, S. Erk, S. Mohnke, L. Pöhland, L. Haddad, O. Grimm, H. Tost *et al.*, Segregation of face sensitive areas within the fusiform gyrus using global signal regression? A study on amygdala resting-state functional connectivity, *Human Brain Mapping* **36**, 4089 (2015).

52. B. T. Yeo, J. Tandi and M. W. Chee, Functional connectivity during rested wakefulness predicts

vulnerability to sleep deprivation, *Neuroimage* **111**, 147 (2015).
53. Z. Qing, Z. Dong, S. Li, Y. Zang and D. Liu, Global signal regression has complex effects on regional homogeneity of resting state fMRI signal, *Magnetic Resonance Imaging* **33**, 1306 (2015).
54. A. Anticevic, M. W. Cole, G. Repovs, A. Savic, N. R. Driesen, G. Yang, Y. T. Cho, J. D. Murray, D. C. Glahn, X.-J. Wang *et al.*, Connectivity, pharmacology, and computation: toward a mechanistic understanding of neural system dysfunction in schizophrenia, *Frontiers in Psychiatry* **4**, p. 169 (2013).
55. A. Kottaram, L. A. Johnston, L. Cocchi, E. P. Ganella, I. Everall, C. Pantelis, R. Kotagiri and A. Zalesky, Brain network dynamics in schizophrenia: Reduced dynamism of the default mode network, *Human brain mapping* **40**, 2212 (2019).
56. J. Li, R. Kong, R. Liégeois, C. Orban, Y. Tan, N. Sun, A. J. Holmes, M. R. Sabuncu, T. Ge and B. T. Yeo, Global signal regression strengthens association between resting-state functional connectivity and behavior, *Neuroimage* **196**, 126 (2019).